ADVANCED VISCOPLASTIC FINITE-ELEMENT STRUCTURAL ANALYSES USING MARC PROGRAM

V.K. Arya[1] and G. R. Halford[2]
NASA-Lewis research Center
Cleveland, Ohio.

Abstract

This paper presents finite element solution methodologies developed at the National Aeronautics and Space Administration (NASA) Lewis Research Center for use with the general purpose finite element program MARC. The solution technologies are illustrated for two viscoplastic models, one developed by Robinson and the other by Freed and Walker. The developed MARC-based finite element solution technologies for these viscoplastic models are then applied to some mutiaxial structural engineering problems (involving thrust chambers and cowl lip). The results are discussed and applicability of the MARC program to the solution of complex, nonlinear structural engineering problems is demonstrated. It is believed that the results from the present work will encourage engineers/researchers for using MARC program for solving complex structural engineering problems encountered in aerospace and other industries.

Introduction

Classical creep-plasticity constitutive models treat creep and plastic strains as independent noninteracting entities. These models are, therefore, incapable of accounting for the observed interactions between creep and plastic strains at high temperatures. Viscoplastic models, however, consider all the inelastic strain (including plasticity, creep, relaxation, etc.) as a single, unified, time-dependent quantity, and thus, automatically include interactions that occur among them. Viscoplastic models, therefore, provide more realistic descriptions of time-dependent inelastic behavior of materials at high temperatures. Viscoplastic models become more realistic when as much material physics as possible is included in the models. This, however, results in complex mathematical frameworks for viscoplastic models. The constitutive differential equations of viscoplastic models that govern the flow and evolution laws are generally highly nonlinear and mathematically stiff. The closed-form solutions for structural engineering problems are virtually intractable when viscoplastic models are used to define the stress-strain relationship. To assess the advantages offered by more realistic viscoplastic models one must, therefore, employ numerical solution methodology involving, for example, the finite element method or the boundary element method.

Toward this aim, this paper presents a review of the finite element solution methodologies developed at the National Aeronautics and Space Administration (NASA) Lewis Research Center for use with the general purpose finite element program MARC [1]. The methodologies, designed for use with viscoplastic models, are demonstrated in this paper for viscoplastic models put forth by Robinson [2] and Freed and Walker [3]. However, because the methodologies are general in nature, these can easily be adapted for use with other viscoplastic models. For completeness, the paper includes brief descriptions of the two viscoplastic models. The methodologies are illustrated by applying them to multiaxial problems.

---

[1] Visiting Associate Professor, The University of Akron, Ohio.
[2] Senior Scientific Technologist, Structures Division.

Viscoplastic Models

Robinson's Viscoplastic Model

Robinson's model [2] employs a dissipation potential to derive the flow and evolutionary laws for the inelastic strain and internal state variables. The model incorporates a single internal state variable representing kinematic hardening. The material behavior is elastic for all the stress states within the dissipation potential and is viscoplastic for the stress states outside. A small displacement and a small strain formulation are employed.

The total strain rate $\dot{\varepsilon}_{ij}$ is decomposed into elastic, $\dot{\varepsilon}_{ij}^{el}$, inelastic $\dot{\varepsilon}_{ij}^{in}$ (including plastic, creep, relaxation, etc.), and thermal $\dot{\varepsilon}_{ij}^{th}$ strain-rate components. Thus

$$\dot{\varepsilon}_{ij} = \dot{\varepsilon}_{ij}^{el} + \dot{\varepsilon}_{ij}^{in} + \dot{\varepsilon}_{ij}^{th} \qquad (i,j = 1,2,3) \qquad (1)$$

The elastic strain rate for an isotropic material is governed by Hooke's law:

$$\dot{\varepsilon}_{ij}^{el} = \frac{1+\nu}{E}\,\dot{\sigma}_{ij} - \frac{\nu}{E}\,\dot{\sigma}_{kk}\,\delta_{ij} \qquad (2)$$

where E is the Young's modulus, ν is the Poisson 's ratio and σ_{ij} is the stress. The repeated subscripts in equation (2) and elsewhere imply summation over their range, and δ_{ij} is the Kronecker delta function. A dot over a symbol denotes its derivative with respect to time t.

The nonisothermal multiaxial inelastic constitutive equations for the model are given below:

Flow Law

$$\dot{\varepsilon}_{ij}^{in} = \begin{cases} \dfrac{AF^{\eta}\,\Sigma_{ij}}{\sqrt{J_2}} & F > 0 \quad \text{and} \quad S_{ij}\,\Sigma_{ij} > 0 \\[2ex] 0 & F \leq 0 \quad \text{or} \quad F < 0 \quad \text{and} \quad S_{ij}\,\Sigma_{ij} \leq 0 \end{cases} \qquad (3)$$

Evolutionary Law

$$\dot{a}_{ij} = \begin{cases} \dfrac{H}{G^{\beta}}\,\dot{\varepsilon}_{ij}^{in} - \dfrac{RG^{m-\beta}}{\sqrt{I_2}}\,a_{ij} & G < G_o \quad \text{and} \quad S_{ij}\,a_{ij} > 0 \\[2ex] \dfrac{H}{G_o^{\beta}}\,\dot{\varepsilon}_{ij}^{in} - \dfrac{RG_o^{m-\beta}}{\sqrt{I_2}}\,a_{ij} & \begin{array}{l} G \leq G_o \\ \text{or} \quad G > G_o \quad \text{and} \quad S_{ij}\,a_{ij} \leq 0 \end{array} \end{cases}$$

$$(4)$$

where

$$F = \frac{J_2}{K^2} - 1 \qquad (5)$$

$$G = \frac{I_2}{K_o^2} \qquad (6)$$

$$J_2 = \frac{1}{2}\,\Sigma_{ij}\,\Sigma_{ij} \qquad (7)$$

$$I_2 = \frac{1}{2}\,a_{ij}\,a_{ij} \qquad (8)$$

$$\Sigma_{ij} = S_{ij} - a_{ij} \qquad (9)$$

$$\left.\begin{array}{l} S_{ij} = \sigma_{ij} - \dfrac{1}{3}\,\sigma_{kk}\,\delta_{ij} \\[2ex] a_{ij} = \alpha_{ij} - \dfrac{1}{3}\,\sigma_{kk}\,\delta_{ij} \end{array}\right\} \qquad (10)$$

Viscoplastic Models

Robinson's Viscoplastic Model

Robinson's model [2] employs a dissipation potential to derive the flow and evolutionary laws for the inelastic strain and internal state variables. The model incorporates a single internal state variable representing kinematic hardening. The material behavior is elastic for all the stress states within the dissipation potential and is viscoplastic for the stress states outside. A small displacement and a small strain formulation are employed.

The total strain rate $\dot{\varepsilon}_{ij}$ is decomposed into elastic, $\dot{\varepsilon}_{ij}^{el}$, inelastic $\dot{\varepsilon}_{ij}^{in}$ (including plastic, creep, relaxation, etc.), and thermal $\dot{\varepsilon}_{ij}^{th}$ strain-rate components. Thus

$$\dot{\varepsilon}_{ij} = \dot{\varepsilon}_{ij}^{el} + \dot{\varepsilon}_{ij}^{in} + \dot{\varepsilon}_{ij}^{th} \qquad (i,j = 1,2,3) \qquad (1)$$

The elastic strain rate for an isotropic material is governed by Hooke's law:

$$\dot{\varepsilon}_{ij}^{el} = \frac{1+\nu}{E}\,\dot{\sigma}_{ij} - \frac{\nu}{E}\,\dot{\sigma}_{kk}\,\delta_{ij} \qquad (2)$$

where E is the Young's modulus, ν is the Poisson 's ratio and σ_{ij} is the stress. The repeated subscripts in equation (2) and elsewhere imply summation over their range, and δ_{ij} is the Kronecker delta function. A dot over a symbol denotes its derivative with respect to time t.

The nonisothermal multiaxial inelastic constitutive equations for the model are given below:

Flow Law

$$\dot{\varepsilon}_{ij}^{in} = \begin{cases} \dfrac{AF^n\,\Sigma_{ij}}{\sqrt{J_2}} & F > 0 \quad \text{and} \quad S_{ij}\,\Sigma_{ij} > 0 \\[2ex] 0 & F \le 0 \quad \text{or} \quad F < 0 \quad \text{and} \quad S_{ij}\,\Sigma_{ij} \le 0 \end{cases} \qquad (3)$$

Evolutionary Law

$$\dot{a}_{ij} = \begin{cases} \dfrac{H}{G^\beta}\,\dot{\varepsilon}_{ij}^{in} - \dfrac{RG^{m-\beta}}{\sqrt{I_2}}\,a_{ij} & G < G_o \quad \text{and} \quad S_{ij}\,a_{ij} > 0 \\[2ex] \dfrac{H}{G_o^\beta}\,\dot{\varepsilon}_{ij}^{in} - \dfrac{RG_o^{m-\beta}}{\sqrt{I_2}}\,a_{ij} & G \le G_o \quad \text{or} \quad G > G_o \quad \text{and} \quad S_{ij}\,a_{ij} \le 0 \end{cases} \qquad (4)$$

where

$$F = \frac{J_2}{K^2} - 1 \qquad (5)$$

$$G = \frac{I_2}{K_o^2} \qquad (6)$$

$$J_2 = \frac{1}{2}\,\Sigma_{ij}\,\Sigma_{ij} \qquad (7)$$

$$I_2 = \frac{1}{2}\,a_{ij}\,a_{ij} \qquad (8)$$

$$\Sigma_{ij} = S_{ij} - a_{ij} \qquad (9)$$

$$\left. \begin{aligned} S_{ij} &= \sigma_{ij} - \frac{1}{3}\,\sigma_{kk}\,\delta_{ij} \\[2ex] a_{ij} &= \alpha_{ij} - \frac{1}{3}\,\sigma_{kk}\,\delta_{ij} \end{aligned} \right\} \qquad (10)$$

In the preceding equation, S_{ij} is the deviatoric stress, and α_{ij} and K are the internal state variables. The variable, α_{ij} called the back stress, accounts for the kinematic hardening, whereas K, taken here to be a constant, is called the drag stress and represents the isotropic hardening of the material. The value of K at the reference temperature is denoted by K_o and the minimum value attainable by G is denoted by G_o. The inequalities in equations (3) and (4) define boundaries across which the flow and evolutionary laws change form discontinuously. To facilitate the numerical computations, these boundaries are smoothed by using a spline function given in the next section. Seven numerical parameters are required to characterize a given material. These parameters are A, n, m, H, R, G_o and $K(K_o)$. The values of these parameters for the copper alloy NARloy-Z, taken from reference 4, are listed in table I.

Spline Function

The discontinuous boundaries in Robinson's viscoplastic model should be smoothed to facilitate numerical computations. This smoothing is achieved by defining a "spline function" P(x) (refs. 2 and 5) on the interval (-1,1) as

$$P(x) = \begin{cases} \dfrac{(1+x)^2}{2} & -1 \leq x < 0 \\[2ex] 1 - \dfrac{(1-x)^2}{2} & 0 \leq x \leq 1 \\[2ex] 1 & x > 1 \\[2ex] 0 & x < -1 \end{cases} \qquad (11)$$

Freed and Walker Model

The viscoplastic model used herein was recently put forth by Freed and Walker [3]. The model contains one scalar internal state variable D, called the drag strength, and an internal variable B_{ij}, called the back stress. The back stress B_{ij} is assumed to be composed of two back stresses that are denoted by B_{ij}^s ; and B_{ij}^ℓ . (A small displacement and a small strain formulation is employed in the model.)

Again as in equation (1), the total strain rate is written as the sum of elastic, inelastic (including plasticity, creep, relaxation, etc.), and thermal strain rate components. The stress σ_{ij} is taken to be related to elastic strain by Hooke's law , equation (2).

The deviatoric total strain rate $\dot{E}_{ij}$ has the following expression

$$\dot{E}_{ij} = \dot{\varepsilon}_{ij} - \frac{1}{3} \dot{\varepsilon}_{kk} \, \delta_{ij} \qquad (12)$$

The back stress B_{ij} is the sum of two back stress components B_{ij}^s and B_{ij}^ℓ,

$$B_{ij} = B_{ij}^s + B_{ij}^\ell \qquad (13)$$

The effective stress Σ_{ij} is defined as

$$\Sigma_{ij} = S_{ij} - B_{ij} \qquad (14)$$

The temperature dependence of the model is mainly contained in the thermal diffusivity function Θ which is defined as

$$\Theta = \begin{cases} \exp(-Q/kT) & T_t \leq T \leq T_m \\[2ex] \exp\left[-\dfrac{Q}{kT_t}\left\{\ln\left(\dfrac{T_t}{T}\right) + 1\right\}\right] & 0 \leq T \leq T_t \end{cases} \tag{15}$$

In equation (15), Q is the activation energy, k is the Boltzmann constant, T is absolute temperature, T_t is transition temperature, and T_m is the melting temperature of the material.

The function Z, the Zener-Hollomon parameter, is defined by

$$Z = A \, \sinh^n\left(\sqrt{J_2}/D\right) \tag{16}$$

where J_2 is defined by equation (7) and A and n are inelastic material constants.

The evolution equations for the internal state variables are

$$\dot{B}^\alpha_{ij} = 2H_\alpha \left(\dot{\varepsilon}^v_{ij} - \frac{B^\alpha_{ij}}{2L_\alpha} I_2\right) \tag{17}$$

where $a = s, \ell$. The strain invariant I_2 is defined by

$$I_2 = \begin{cases} \Theta Z & \text{if } J_2 < K^2 \\[1ex] P_{ij} \dot{E}_{ij}/P^M & \text{otherwise} \end{cases} \tag{18}$$

In equation (18)

$$P_{ij} = \frac{E}{2(1 + \nu)} \frac{\Sigma_{ij}}{\sqrt{J_2}} \tag{19}$$

and $\dot{E}_{ij}$ is defined by equation (12). Also

$$P^M = \frac{E}{2(1 + \nu)} + \Sigma_\alpha \frac{H_\alpha}{L_\alpha}\left(L_\alpha - \frac{1}{2} B^\alpha_{ij} \frac{\Sigma_{ij}}{\sqrt{J_2}}\right) \tag{20}$$

117

The functions K, H_α and L_α in the above equations are given by

$$K = (C - D_0) (C + D_0)/4 \delta C \qquad (21)$$

$$H_s = \frac{E}{2(1 + \nu)} \qquad H_\ell = \frac{E}{2(1 + \nu) H_0} \qquad (22)$$

and

$$L_s = f \frac{(C - D) (D - D_0)}{\delta C} \qquad L_\ell = (1 - f) \frac{(C - D) (D - D_0)}{\delta C} \qquad (23)$$

in which C, δ, H_o and f are material constants and D_o denotes the minimum value that the drag strength D can take for a given material.

The drag strength D evolves according to the following equation

$$\dot{D} = h (I_2 - \Theta r) \qquad D_0 \leq D \leq D_{max} \qquad (24)$$

where

$$D_{max} = (C + D_0)/2 \qquad (25)$$

and

$$r = A \sinh [(D - D_0)/\delta C]^n \qquad (26)$$

The function h is defined as

$$h = h_D \left[\frac{(D - D_0)/\delta C}{\sinh\{(D - D_0)/\delta C\}} \right]^m \qquad (27)$$

where

$$h_D = \begin{cases} h_1 & T_t \leq T \leq T_m \\ h_0 - \dfrac{h_0 - h_1}{T_t} T & 0 < T \leq T_t \end{cases} \qquad (28)$$

In equation (28), h_o and h_l are material constants.

118

In addition to elastic material constants, the shear modulus μ, Poisson's ratio ν, and the coefficient of thermal expansion α, the above viscoplastic model has 13 inelastic material constants: A, C, δ, D_o f, H_o, h_o, h_l, m, n, Q, T_m and T_t. The values of these constants taken from Freed and Walker [3] are listed in Table II.

MARC (Finite Element) Analyses

Robinson's Viscoplastic Model - *Cylindrical Thrust Chamber Liner Problem*

<u>Background Information and Relevance</u>

Progressive deformation and thinning of coolant-channel walls in high-pressure, reusable rocket thrust chambers have been observed during operation of engines such as the Space Shuttle Main Engine (SSME). This inelastic ratcheting behavior is attributed to the significant, thermally induced inelastic strains that occur in the hot-gas-side wall during cyclic firing as well as to the biasing pressure differential across the wall. After numerous thermal cycles, ratcheting strains accumulate to the extent that cracks form (i.e., failure occurs) in the cooling passage wall. Numerous analytical and experimental studies have been undertaken in recent years to examine this phenomenon [7-10].

For an accurate estimation of the life of thrust chambers a realistic inelastic stress-strain analysis is required. Conventional inelastic analyses of components treat the plastic (time- independent) and creep (time-dependent) strains as independent noninteracting entities; these are inadequate for this application, since at elevated temperatures, interactions are known to exist between plastic and creep strains within metallic materials [11]. Alternatively, unified viscoplastic analyses provide realistic descriptions of high-temperature inelastic behavior of materials, in that all inelastic strains (e.g., creep, plastic, relaxation, and their interactions) are accounted for as a single, time-dependent quantity.

In the present part of the paper results of a unified viscoplastic finite element stress-strain analysis of an experimental thrust chamber composed of NARloy-Z, a copper-based alloy are presented. The objective of this study was twofold: i) to qualitatively predict the experimentally verified thinning of the cooling passage and the so-called "dog house" effect [7] by using a viscoplastic model put forth by Robinson [2]; and ii) to investigate the influence of loading cycle duration on the structural response of the cylindrical chamber. To achieve the second objective, two types of thermomechanical loading cycles (see table III) were employed-one corresponding to the experimental simulations and one being more typical of the cycle seen by the SSME.

A cross section of the experimental cylinder wall, which contains 72 cooling channels, is shown in figure 1. The shaded area in the figure depicts the segment of the component that was modeled to perform the thermal and structural analyses. The cyclic thermal and pressure loadings [9] shown in table III lead progressively to a deformed segment that results in the "dog house" effect [8]. Figure 2, which shows this dog house, illustrates how the component fails by thinning of the cooling channel wall and eventual tensile rupture. Further details of experiments and apparatus can be found in references 7 and 8.

Finite Element Model

Figure 3 depicts the finite element model used for the thermal and stress analyses. It consists of 35 elements and 54 nodes . To facilitate a quasi-three-dimensional analysis, generalized plane strain elements were used to model the smallest repeating segment of the cylinder wall. Because the wall was symmetrical, only one-half of a cooling channel was modeled.

Thermal Analysis

In reference 7, the thermal analyzer program SINDA (ref. 12) was used to perform the thermal analysis and to generate the time-dependent cross-sectional temperatures. Time-dependent hot-gas-side and coolant-side boundary conditions were input to the SINDA program to obtain the temperature profile as a function of time. To

estimate the quantities for which no experimental data were available, some assumptions and approximations were made in the thermal analysis. Complete details of the thermal analysis are provided in reference 7.

Finite Element Analysis

By employing the finite element program MARC (ref. 1) and a numerical solution procedure put forth by Arya et al. (refs. 13 and 14), a stress-strain analysis of the cylindrical thrust chamber was performed. A self-adaptive integration strategy, based on the explicit forward Euler method and described in reference 15, was employed for the time integration of the nonlinear and mathematically "stiff" constitutive equations of the viscoplastic model. The integration strategy is easy to implement, and it has been employed successfully for the solution of problems involving complex geometries and loadings (refs. 6 and 16). The finite element thermostructural analysis was performed with the time dependent temperature distribution obtained from the thermal analysis described in the preceding section. Time-varying nodal temperatures and elemental pressure loadings were applied to trace the loading cycles of table III. Two loading cycles of different durations were used for numerical computations. The short cycle of 3.S-sec duration corresponded to the loading cycles of the experiments. The extended loading cycle of 485. l-sec duration was typical of SSME operation. The latter cycle offered the opportunity to study the effects of time dependent creep deformation on the structural response of the cylindrical chamber liner. The nonlinear variations in the temperature-dependent material properties were accounted for in the computations. The temperature distribution obtained from the thermal analysis described in the preceding section was used for the stress analysis.

Results and Discussion

Short Loading Cycle

The circumferential (x-direction) stress distribution in the segment of the component used for the finite element analysis is shown in figure 4 at the completion of the 1st and 12th short loading cycles. The circumferential stress is tensile and, in general, decreases with the number of loading cycles. The radial (y-direction) stress distribution is shown in figure 5; here some redistribution of the radial stress with loading cycles is observed in the upper part of the segment. In the lower part of the segment the radial stress remains unaltered at some points, but it increases in magnitude at other points of the segment; for example, in the vicinity of point B.

The circumferential (x-direction) and radial (y-direction) mechanical strain distributions in the segment at the end of the 1st and 12th short loading cycles are shown in figures 6 and 7, respectively. The circumferential strains are compressive everywhere and are found to increase in magnitude in the neighborhood of points A and D with the number of loading cycles. The radial (y-direction) strains are compressive in the segment at the end of the first cycle. Comparison of the radial strain distributions in the segment at the end of the 1st and 12th loading cycles (see fig. 7) shows that the radial strain becomes less compressive with the loading cycles. The predicted shapes of the segment after the 1st and 12th short loading cycles are shown in figure 8. These figures are magnifed by a factor of 50 so that the small difference in deformity can be seen.

Extended Loading Cycle

The circumferential (x-direction) and radial (y-direction) stress distributions in the segment at the end of the 1st and 12th extended loading cycles are shown in figures 9 and 10, respectively. The circumferential stress is tensile and decreases with the loading cycles. The radial stress either remains unaltered or increases in magnitude with the loading cycles. A comparison of the radial and circumferential stress distributions for the short (figs. 4 and 5) and the extended (figs. 9 and 10) loading cycle shows that , in general , the stress values for the extended loading cycles are lower in magnitude than the corresponding values for the short loading cycles.

Figures 11 and 12 portray the circumferential (x-direction) and radial (y-direction) strain distributions in the segment at the completion of the 1st and 12th extended loading cycles. The circumferential strain increases in magnitude in the lower right part of the segment in the neighborhood of point D, whereas it decreases in magnitude in the lower section of the component in the vicinity of point B and increases in the neighborhood of point A. The radial strain becomes less compressive with the loading cycles at all points of the segment. The radial

strain in the neighborhood of point D changes to tensile (12th cycle) from compressive (1st cycle). A comparison of the strain distribution for the 12th short (fig. 6) and extended (fig. 11) loading cycles reveals that, for the extended cycle, the magnitude of the circumferential strain is lower in the vicinity of points A and B and higher in the vicinity of points C and D than it is for the short cycle. The radial strain for the 12th extended loading cycle (fig. 12) is found to be the same or lower in magnitude than that for the short loading cycle (fig. 7) at the corresponding points of the segment - except near point B, where the trend is reversed.

Figure 13 depicts the deformed shapes of the segment after the 1st and 12th extended loading cycles. This figure shows noticeable deformation of the coolant-channel wall after the 12th extended loading cycle.

Figure 14 displays the circumferential (x-direction) displacements at point C of the segment (see inset) as a function of the number of cycles for both the short and extended loading cycles. The displacement values plotted are the values at the completion of the corresponding loading cycle. Since point D of the segment (which lies in the same horizontal plane as the point C) is constrained in this direction, the values shown in figure 14 also give the change in thickness between points C and D. A comparison of the curves for the short and extended cycles reveals that, for the extended cycle, there is a greater thinning across the section CD of the segment. This fact is supported by examination of the circumferential strain ranges across the section CD for the short and extended loading cycles. Since the strain range for the extended cycle is larger (and compressive), greater thinning of the channel wall across section CD is implied for the extended cycle.

The radial (y-direction) displacements at two locations of the segment (designated by points A and B in the inset) are shown in figure 15. The displacement values are plotted with respect to the number of cycles. Note that the displacement values at both locations A and B are higher in magnitude for the extended loading cycle. This means that the coolant channel wall bulges out more for the extended cycle than for the short loading cycle. The difference in the displacement values at points A and B is the change in wall thickness (thinning) across the section AB of the segment. The absolute value of this difference, denoted by Δd, is plotted in figure 16 as a function of the number of cycles. It is interesting to note that the change in wall thickness of the coolant channel (thinning) for the extended loading cycle is smaller than that for the short loading cycle. Close examination of figures 7 and 12 reveals that at the end of 12th cycle the radial strain range across the section AB of the segment is smaller for the extended cycle than it is for the short cycle. The strains are compressive. This small (compressive) radial strain range indicates a smaller thinning of the coolant-channel wall per cycle for the extended cycle history. Since, for the extended cycle, (1) the displacement values are higher in the radial direction and (2) the wall thinning across section AB is smaller in the radial direction and larger across section CD in the circumferential direction than that for the short loading cycle, the failure modes and their location in the segment may be different for the two types of loading cycles.

The circumferential (x-direction) stress distribution in the segment at the hot phase of the 1st and 12th extended loading cycles is shown in figure 17. Figure 18 depicts the corresponding temperature distribution. We can see from figure 17 that, at the hot phase of the 12th extended cycle, the maximum (in magnitude) circumferential stress is compressive and occurs across section AB. The circumferential stress at the completion of the same cycle (fig. 9) is also at a maximum across section AB, but it is tensile. Since a compressive stress cannot cause the radial cracks seen in the experiments (fig. 3), the cracks (and hence the failure of the segment) are unlikely to occur at the hot end of the cycle. The cracks (and failure) may occur only at the end of the cycle or at the beginning of the next cycle, since the circumferential stress then becomes tensile.

Figure 19 shows the predicted shapes of the NARloy-Z segment at the end of 24th short and the 4th extended loading cycles. By employing Robinson's viscoplastic model and using the MARC finite element program, we were able to predict the "dog house" effect observed in the experiments of reference 3 (see fig. 2).. The predicted shape for the copper thrust chamber at the end of the fourth short loading cycle is also shown in figure 19. This figure shows a larger deformation for the copper chamber than for the NARloy-Z chamber, as would be expected since copper is a softer material than NARloy-Z.

Freed and Walker Viscoplastic Model - *Cowl Lip Problem*

Background and Relevance

To demonstrate the feasibility of performing complex structural analyses using a viscoplastic model, the finite element implementation of Freed and Walker's viscoplastic model was applied to a sample structural

component used in the aerospace industry. The component, called a cowl lip, is part of the leading edge of a hypersonic aircraft engine inlet. To achieve high inlet aerodynamic performance for proposed hypersonic flight between Mach 3 and 25, not only must the high heat flux and high heating rates be tolerated, but distortions caused by thermal warping of the structure must also be minimized. Consequently, the need arises for the development of actively cooled leading edges fabricated from specialized materials as well as innovative cooling enable a structure to withstand the severe thermal loading conditions. The details of different cooling concepts proposed under a NASA Lewis sponsored program, called COLT (Cowl Lip Technology Program), were presented by Melis and Gladden [17]. In this paper, a cooling concept, called the parallel flow concept, was investigated. In this concept, the coolant channels are laid parallel to the leading edge of the cowl lip (fig. 20), and the coolant is flowed through them to contain the temperature of the component. The viability of the parallel flow concept is investigated by performing the structural analysis with the finite element implementation of Freed and Walker's viscoplastic model.

The cowl lip geometry is shown in figure 20. The dimensions of the cowl lip are 15.2 by 3.8 by 0.84 cm. However, for the finite element analysis only the 5-cm central portion of the cowl lip was modeled to avoid end effects that would be difficult to quantify. The finite element mesh for this central portion was constructed by Melis and Gladden [17]. The model was made up of 3294 solid, 8-noded hexagonal elements and has 4760 nodes. A large number of finite elements was required to deal with the severity of thermal loadings and gradients. Note from figure 21 that the temperature at a critical location of the component rises from 21 to 758 °C in only 0.75 sec, indicating the severity of loading. However, because of the geometrical symmetry of the component, one need consider only half of the component for the finite element analysis, which results in a considerable savings in CPU time.

The steady-state temperature distribution in the component was obtained from Melis and Gladden [17], which includes detailed results of a steady-state heat transfer analysis that was performed to obtain the steady-state temperature distribution in the cowl lip. Figure 21 shows this temperature distribution in the cowl lip. Figure 22 depicts the thermal loading cycle used in finite element analysis. The transient temperature distribution was obtained by using a linear interpolation technique. The highest temperatures in the component occur along the leading edge of the cowl lip. The temperature values thus obtained for thermal loading cycle were used to perform the cyclic finite element analysis of the cowl lip

Results and Discussion

The most significant results of the cowl lip problem were obtained by plotting the stresses and strains along the leading edge, that is, the z-direction in figures 23 through 27. The stress distribution in the z-direction at 0.75 s is exhibited in figure 23, which shows the maximum (compressive) stress occurring at the leading edge of the cowl lip. Figure 24 displays the stress distribution in the z-direction of the cowl lip at 2.25 s. A comparison of these figures reveals significant redistribution of stress in the component as a result of inelastic deformation. The stress along the leading edge is now seen to be tensile. This shows that viscoplastic models are capable of picking the redistribution of stress caused by inelastic deformation even for a short duration of 1.5 s. Note that a nonunified elastic-plastic-creep analysis of this component performed by Arya et al. [18] was unable to capture this redistribution of stress.

The strain distributions in z-direction in the cowl lip at 0.75 s and 2.25 s are shown in figures 25 and 26, respectively. These figures show the values of total strain at different locations of the cowl lip. The compressive inelastic strain along the leading edge accumulates (increases) with time, which makes the total (tensile) strain along the leading edge decrease. This can be observed by comparing figures 25 and 26. For example, the total strain along the edge of the cowl lip reduces from a value of 0.00491 at 0.75 s to a value of 0.00483 at 2.25 s. The deformed shape of the segment at 0.75 s is plotted in figure 27. For easier examination, the displacements in this figure are magnified by a factor of 1000. This figure shows that the maximum deformation of the segment occurs near point A. The component thickens in this region, which will lead to distortion of the coolant channel configuration. This thickening of the leading edge will also require more cooling down time, and this will lead to an early failure of the component. This indicates that, for the cowl lip problem, the parallel flow concept is not a particularly advantageous concept.

122

Summary

MARC finite element program based solution technologies are described for viscoplastic models put forth by Robinson and Freed and Walker. It is illustrated for the finite element program MARC. However, the generality of methodologies makes them easily adaptable to any other finite element program. The viability of methodology ia demonstrated by applying it to some multiaxial problems.. The advantages of using an advanced viscoplastic model for nonlinear structural analyses in conjunction with MARC program are established. The results from the current viscoplastic finite element analyses illustrate the feasibility of advanced viscoplastic models for estimating the high temperature inelastic response of structural engineering components for an accurate life prediction and estimation. This should encourage researchers and designers to employ advanced viscoplastic models for better and rational designs of structural components.

References

1. MARC General Purpose Finite Element Program. Marc Analysis Research Corporation, Palo Alto, CA, 1988.
2. Robinson, D.N.; and Swindeman, R.W.: Unified Creep-Plasticity Constitutive Equations for 2 Cr-lMo Steel at Elevated Temperature. ORNL/TM-8444, Oct. 1982.
3. Freed, A.D., Walker, K.P. Viscoplasticity with creep and plasticity bounds. Int. J. Plast. 9, 2, 213-242, 1993.
4. Arnold, S.M.: Effects of State Recovery on Creep Buckling Induced by Thermomechanical Loading. Ph.D. Thesis, Akron University, 1987.
5. Arya, V.K.; and Kaufman, A.: Finite Element Implementation of Robinson's Viscoplastic Model and its Application to Some Uniaxial and Multiaxial Problems. Eng. Comput., vol. 6, Sept. 1989, pp. 537-547.
6. Arya, V.K.: Nonlinear Structural Analysis of Cylindrical Thrust Chambers Using Viscoplastic Models. NASA CR-185253, 1990.
7. Quentmeyer, R.L.: Thrust Chamber Thermal Barrier Coating Techniques. NASA TM- 100933, 1988.
8. Quentmeyer, R.L.: Experimental Fatigue Life Investigation of Cylindrical Thrust Chambers. NASA TM X-73065, 1977.
9. Armstrong, M.H.: Structural Analysis of Cylindrical Thrust Chambers- Final Report- Vol. I. NASA CR-159522, 1979.
10. Armstrong, M.H.: Structural Analysis of Cylindrical Thrust Chambers- Final Report-Vol. 11. NASA CR-165241, 1981.
11. Pugh, C.E.: Background Information for Interim Methods of Inelastic Analysis for High-Temperature Reactor Components of 2Cr-lMo Steel. ORNL/TM-5226, 1976.
12. Smith, I.P.: Systems improved Numerical Differencing Analyzer (SINDA): User's Manual. TRW Systems Group, Redondo Beach, CA, TRW- 14690 H001-R0 00, Apr. 1971.
13. Arya, V.K.: Analytical and Finite Element Solutions of Some Problems Using a Viscoplastic Model. Comp. Struct., vol. 33, no. 4, 1989, pp. 957-967.
14. Arya, V.K.: Application of Finite-Element-Based Solution Technologies for Viscoplastic Structural Analyses. NASA CR-185196, 1990.
15. Arya, V.K.; Hornberger K.; and Stamm, H.: On the Numerical Integration of Viscoplastic Models-High Temperature Materials. Report KFK-4082, May 1986.
16. Arya, V.K.: Finite Element Analysis of Structural Components Using Viscoplastic Models With Application to a Cowl Lip Problem. NASA CR-185189, 1990.
17. Melis, M.E., Gladden, H.J.: Thermostructural analysis with experimental verification in a high heat flux facility of a simulated cowl lip. Structures, Structural Dynamics and Material Conference. 29th Pt. 1. AIAA, New York, 106-115, 1988.
18. Arya, V.K., et al., : Finite element elastic-plastic-creep and cyclic life analysis of a cowl lip. Int. J. Fatigue Fract. Eng. Mater. Struct. 14, 10, 967-977, 1991.

TABLE I.—VALUES OF MATERIAL PARAMETERS[a] FOR ROBINSON'S MODEL

cf. 8.]

Parameter	Value
A	1.385×10^{-8}
n	4
m	4.365
β	$0.533 \times 10^{-6}\, T^2 + 0.8$
Q_o	40 000
T_o	811 K (1000 °F)
G_o	0.04
K^2	$69.88 - 0.067\, T$
K_o	$K(T_o)$
H	$(1.67 \times 10^4)(6.895)^{\beta+1}/(3K_o^2)$
R	$(2.19 \times 10^{-3})(6.895)^{1+\beta-m}(3\,K_o^2)^{m-\beta}$ $\times \exp\left[Q_o \left(\dfrac{1}{T_o} - \dfrac{1}{T} \right) \right]$
E	$1.47 \times 10^5 - 70.5 \times T$
ν	0.34

[a]Units are as follows: T is in Kelvin; n, m, β, and G_o are unitless; and the other parameters are consistent with the units of MPa and hr.

TABLE II.—MATERIAL CONSTANTS FOR COPPER

[$\mu = \mu_0 + \mu_1 T$; T is in degrees Kelvin; $D_0 = C/100$; $\delta = 0.035$; $T_t = 0.5\, T_m$.]

Constant	Unit	Value
α	K^{-1}	18×10^{-6}
μ_0	MPa	43 000
μ_1	MPa/K	-17
ν	-----	0.36
A	s^{-1}	2×10^7
C	MPa	13
f	-----	0.75
H_0	-----	20
h_0	MPa	50
h_ℓ	MPa	15
m	-----	0.5
n	-----	4.5
Q	J/mol	200 000
T_m	K	1356

TABLE III.—CYCLIC TEMPERATURE AND PRESSURE LOADING HISTORIES

Fr ...

(a) Duration of Regions

Region	Cycle time, sec	
	Short	Extended
I	0.10	22.50
II	.90	.90
III	.80	180.00
IV	.45	.45
V	1.25	281.25
Total cycle time	3.50	485.10

Typical Cycle History
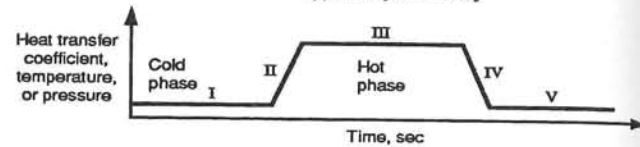
(b) Cycle Phase

	Cold	Hot
Hot-gas-side heat transfer coefficient, W/cm^2-K (Btu/in.^{2}-sec-R)	0	2.02 (0.00685)
Hot-gas-side adiabatic wall temperature, K (°R)	278 (500)	3364 (6055)
Hot-gas-side wall pressure, kN/m^2 (psia)	96.5 (14.0)	2780 (403)
Coolant-side heat transfer coefficient, W/cm^2-K (Btu/in.^{2}-sec-R)	10.2 (0.0345)	4.83 (0.0164)
Coolant-side bulk temperature, K (°R)	28 (50)	50 (90)
Coolant-side wall pressure, kN/m^2 (psia)	5100 (740)	6550 (950)
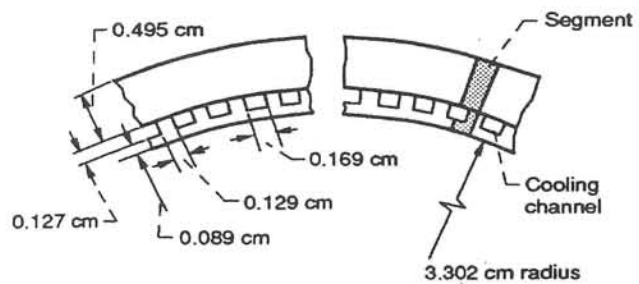
Fig. 1 Cylinder wall cross section showing analyzed segment and dimensions.
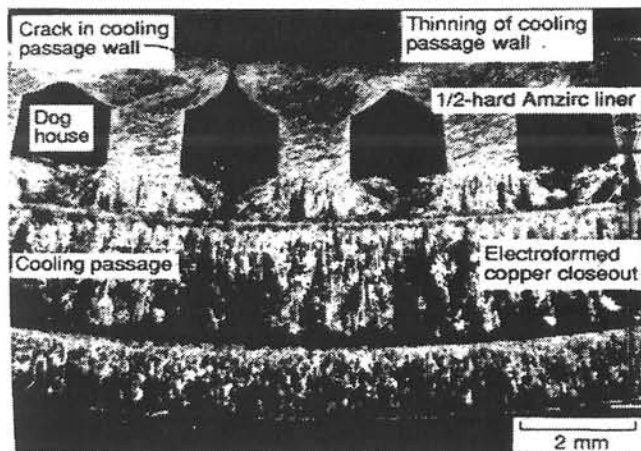
Fig. 2 Cross section of 1/2-hard amzirc cylinder at the throat plane after 393 thermal cycles.
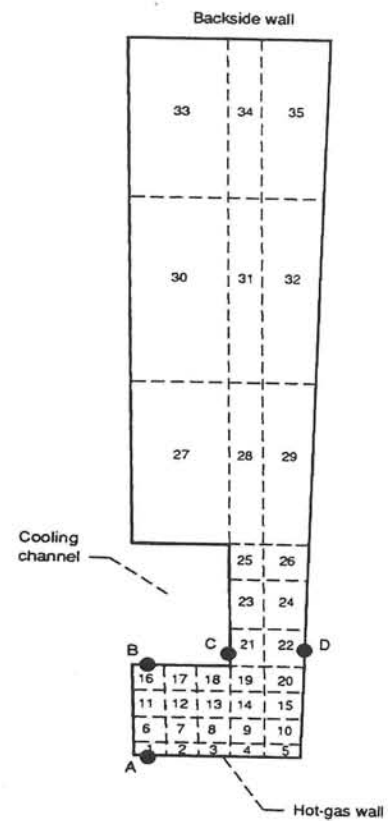
Fig. 3 Finite element model for cylindrical thrust chamber, 35 elements; 54 nodes.
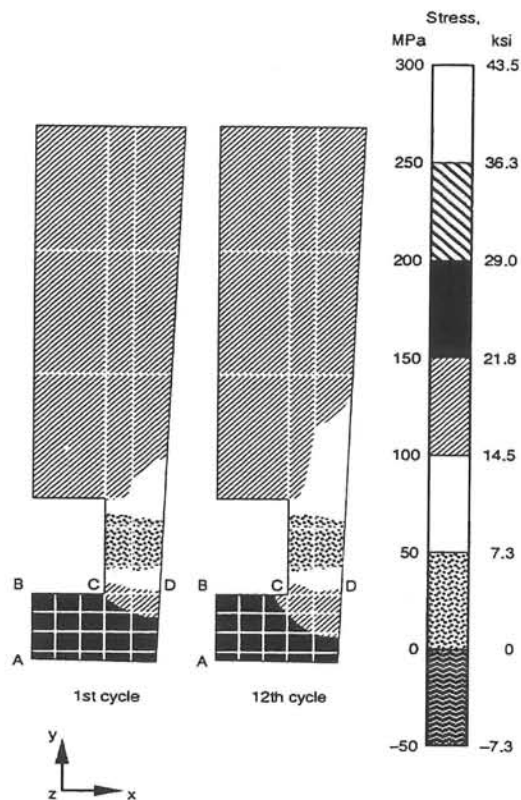
Fig. 4 Short cycle circumferential (x-direction) stress distribution in segment.
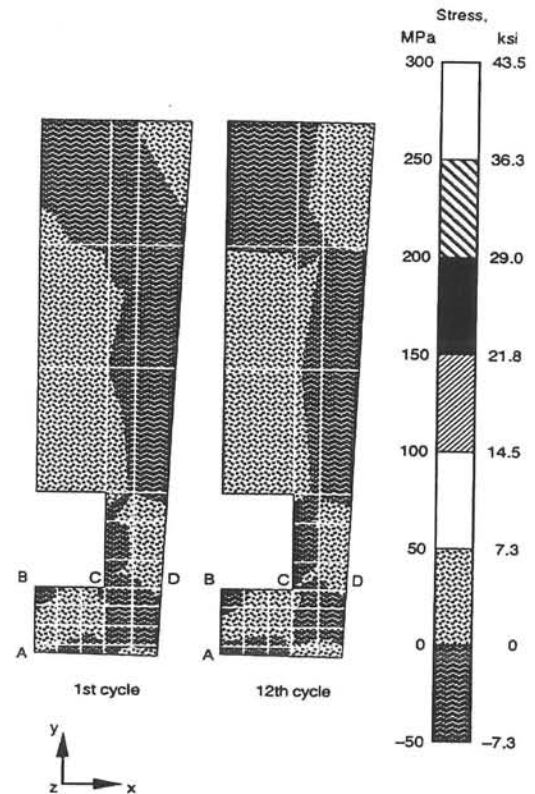
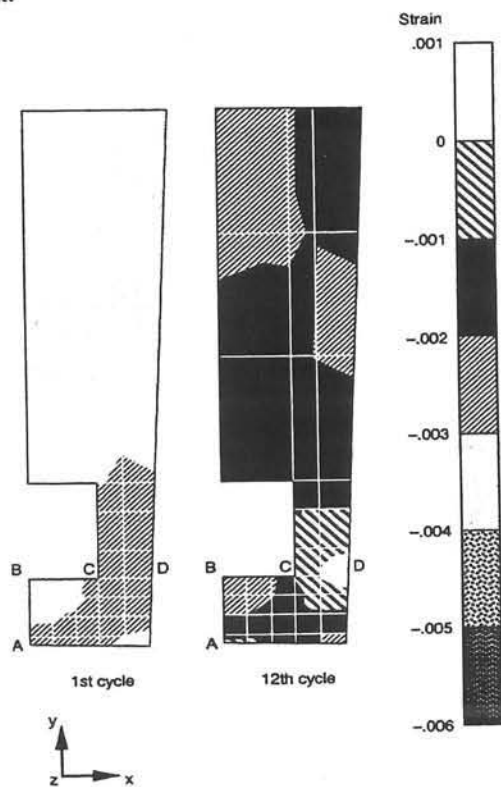Fig. 5 Short cycle radial (y-direction) stress distribution in segment.

125
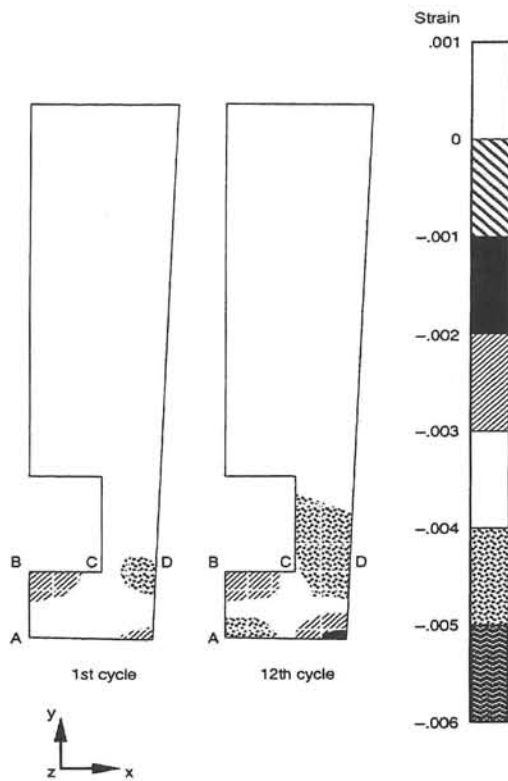
Fig. 6 Short cycle circumferential (*x*-direction) strain distribution in segment.
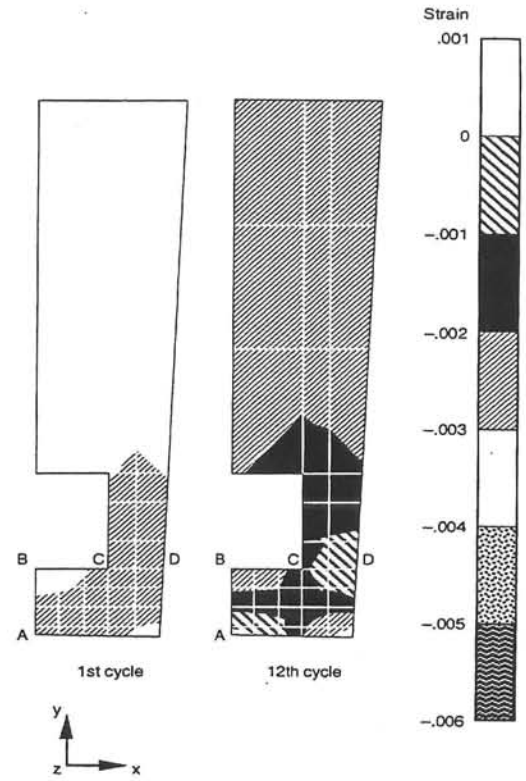
Fig. 7 Short cycle radial (*y*-direction) strain distribution in segment.
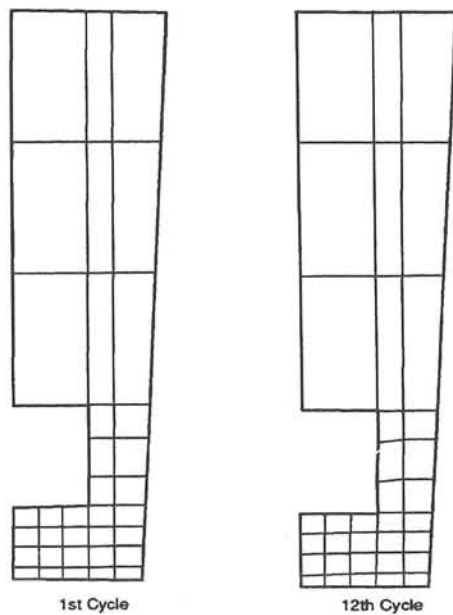
Fig. 8 Predicted shapes of segment after different short cycles (magnification factor ≈ 50).
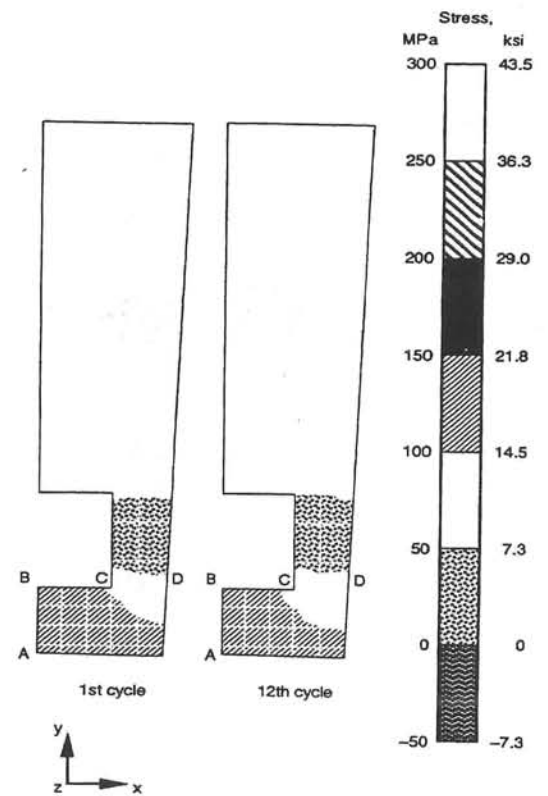
Fig. 9 Extended cycle circumferential (*x*-direction) stress distribution in segment.

126
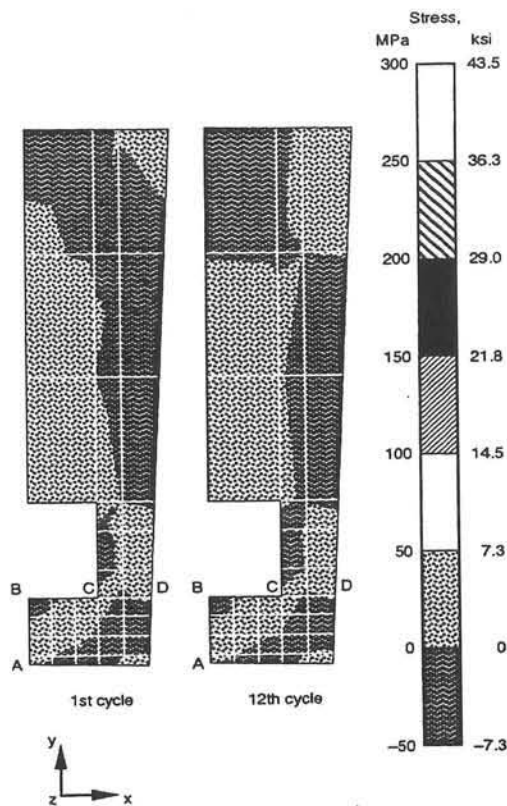
Fig. 10 Extended cycle radial (*y*-direction) stress distribution in segment.

Fig. 11 Extended cycle circumferential (*x*-direction) strain distribution in segment.

Fig. 12 Extended cycle radial (*y*-direction) strain distribution in segment.
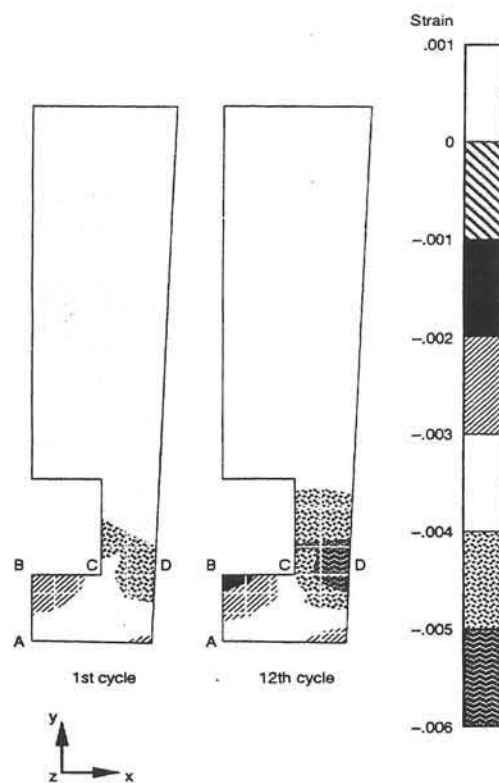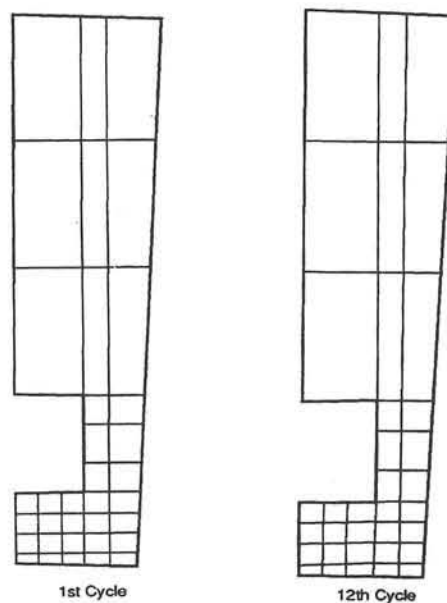
Fig. 13 Predicted shapes of segment after different cycles (extended cycle; magnification factor ≈ 50).

127
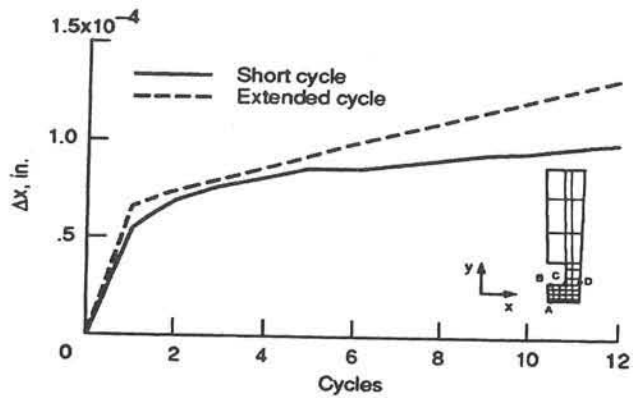
Fig. 14 Decrease in circumferential thickness of segment wall at point C for both short and extended cycles.
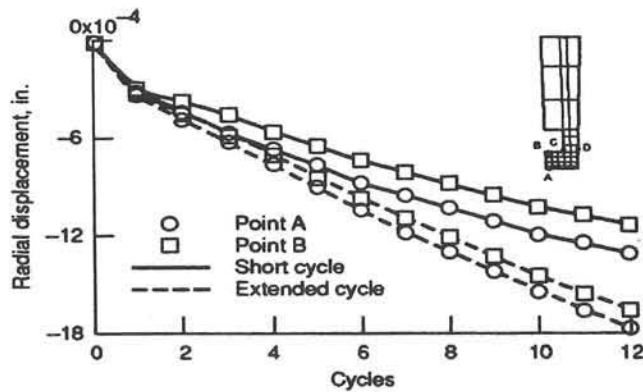
Fig. 15 Radial displacement of points A and B.
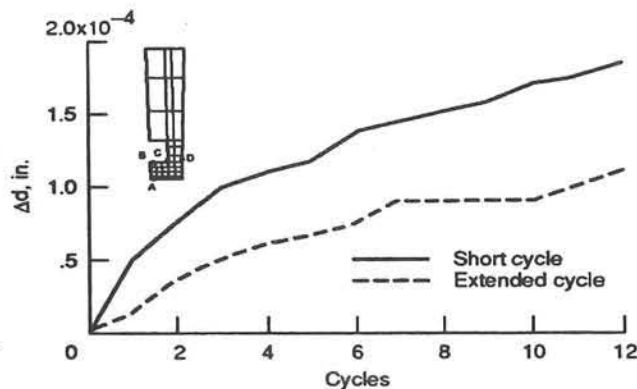
Fig. 16 Decrease in radial thickness across plane AB of segment, for both short and extended cycles.

1st cycle   12th cycle
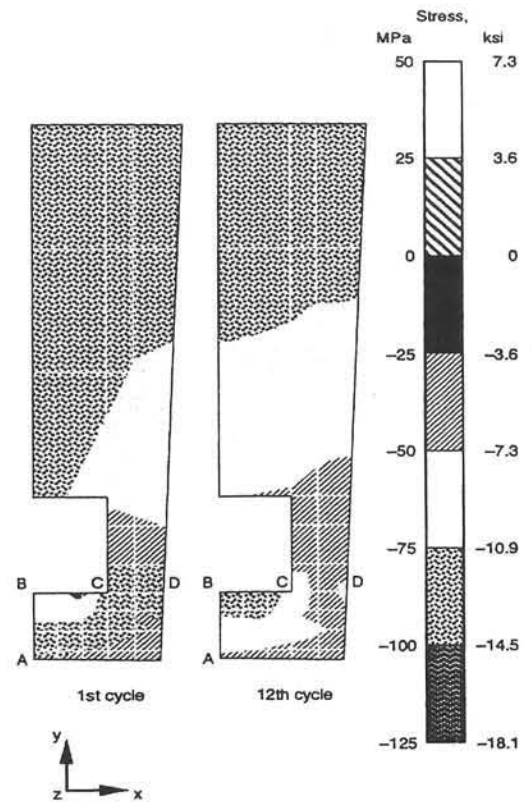
Fig. 17 Extended cycle circumferential (x-direction) stress distribution in segment, for hot phase of cycle.

1st cycle   12th cycle
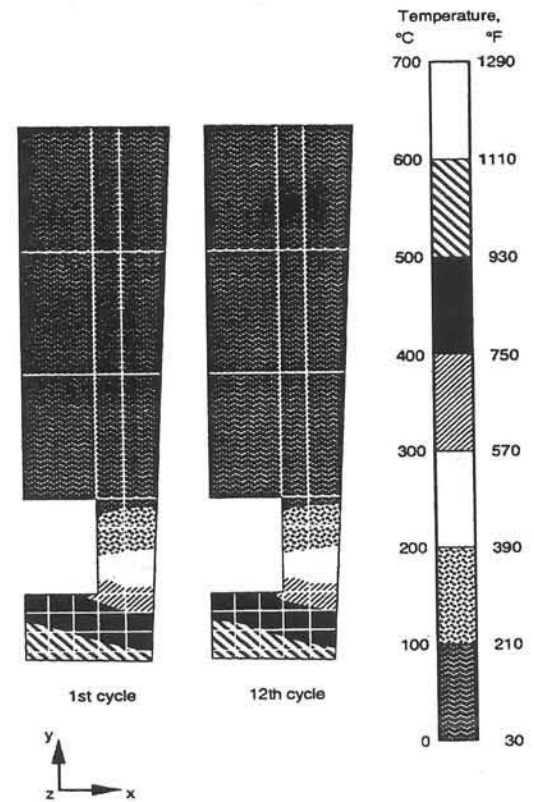
Fig. 18 Extended cycle temperature distribution in segment, for hot phase of cycle.

NARloy-Z (24th short cycle)   NARloy-Z (4th extended cycle)   Copper (4th short cycle)
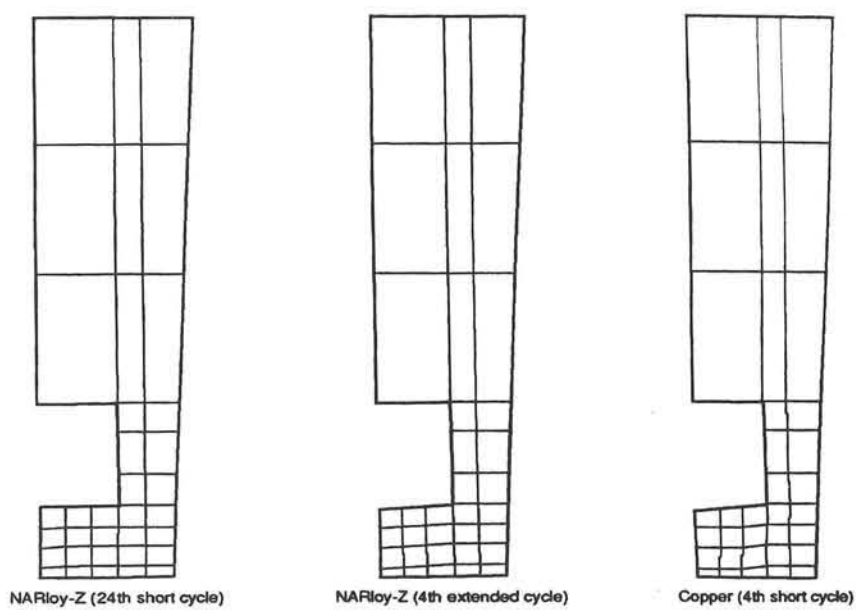
Fig. 19   Comparison of predicted shapes of segments after different cycles (magnification factor $\approx$ 50).
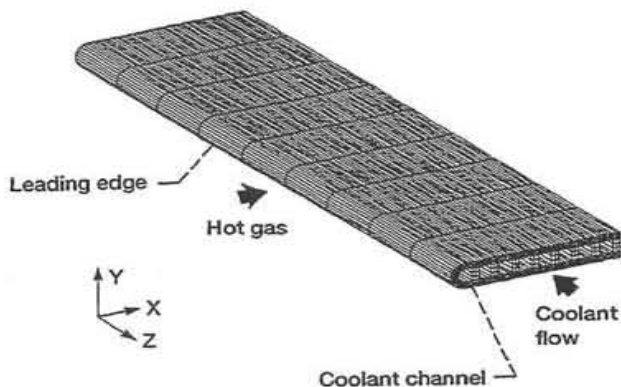
Figure 20 .—Cowl lip finite element model (3294 elements; 4760 nodes).
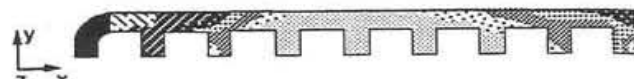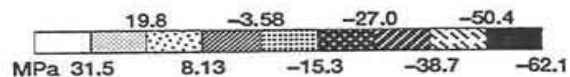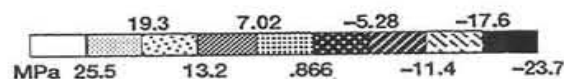

Figure 23 .—Stress in the cowl lip at 0.75 s; z-component.

Figure 24 .—Stress in the cowl lip at 2.25 s; z-component.

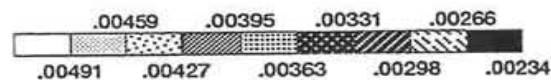Figure 21 .—Steady-state temperature distribution in the cowl lip.

Figure 25 .—Strain in the cowl lip at 0.75 s; z-component.
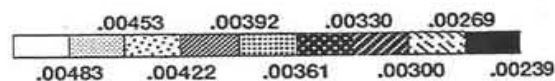
Figure 26 .—Strain in the cowl lip at 2.25 s; z-component.
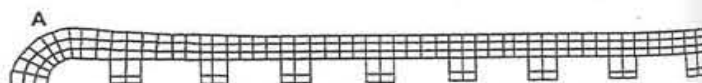

Figure 22 .—Thermal loading cycle.

Figure 27 -Deformed shape of the segment at 0.75 s. (For easier examination, this deformation is magnified by a factor of 1000.)